Title
Cu-Ag Tandem Catalysts for High-Rate CO2 Electrolysis toward Multicarbons

Journal
Joule, 4(8)

ISSN
2542-4785

Authors
Chen, Chubai
Li, Yifan
Yu, Sunmoon
et al.

Publication Date
2020-08-01

DOI
10.1016/j.joule.2020.07.009

Peer reviewed

Cu-Ag tandem catalysts for high-rate CO_2 electrolysis towards multi-carbons

Chubai Chen[1, 3], Yifan Li[1, 3], Sunmoon Yu[2, 3], Sheena Louisia[1, 3], Jianbo Jin[1], Mufan Li[3], Michael B. Ross[1, 5], Peidong Yang[1, 2, 3, 4, 6 *]

[1] Department of Chemistry, University of California, Berkeley, California 94720, United States.

[2] Department of Materials Science and Engineering, University of California, Berkeley, California 94720, United States.

[3] Chemical Sciences Division, Lawrence Berkeley National Laboratory, Berkeley, California 94720, United States.

[4] Kavli Energy NanoScience Institute, Berkeley, California 94720, United States.

[5] Department of Chemistry, University of Massachusetts, Lowell, Massachusetts 01854, United States.

[6] Lead Contact

Correspondence: * p_yang@berkeley.edu

Summary: Electrochemically upgrading CO_2 to carbon-neutral multicarbons (C_{2+}) is a promising technology for CO_2 recycling and utilization. Since such transformations involve multiple elementary steps, a tandem strategy becomes attractive as catalysts can be optimized for specific reaction steps independently. Related strategies have been demonstrated under low working current densities; however, the applicability of a tandem strategy towards high-rate CO_2 electrolysis to C_{2+} is unknown. Here, we demonstrate that a Cu-Ag tandem catalyst can enhance the multicarbon production rate in CO_2RR by decoupling high-rate CO_2 reduction to CO on Ag and subsequent CO coupling on Cu. With the addition of Ag, the partial current towards C_{2+} over a Cu surface increased from 37 mA/cm^2 to 160 mA/cm^2 at -0.70 V vs RHE in 1M KOH while no mutual interference between two metals was observed. Moreover, the normalized intrinsic activity of C_2H_4 and C_2H_5OH in the tandem platform under CO_2 reduction conditions is significantly higher than Cu alone under either pure CO_2 or CO atmosphere. Our results indicate that the CO-enriched local environment generated by Ag can enhance C_{2+} formation on Cu beyond CO_2 or CO feeding, suggesting possible new mechanisms in a tandem three-phase environment.

1. Introduction

CO_2 electrolysis is a promising technique for CO_2 recycling and utilization[1-2], offering carbon-neutral chemical feedstocks[3] for downstream applications. Electrochemical CO_2RR towards single carbon products have achieved enormous progress[4], especially for carbon monoxide[5-9]. However, in the periodic table, copper (Cu) is the only metal that can efficiently catalyze CO_2 to multicarbon products (C_2H_4, C_2H_5OH, CH_3COOH, n-C_3H_7OH, etc.), which was firstly reported by Hori and co-workers[10]. Since multicarbon products are higher-value and energy concentrated[1, 3], widespread attention is paid to the unique catalytic property of the Cu surface. Both theoretical[11] and experimental[12] works demonstrate that sluggish C-C coupling kinetics over a pure Cu surface impedes industrial level production of multicarbon products. Thus, various multicomponent catalyst design principles have been utilized to improve the catalytic performance of Cu-containing catalysts, such as alloy formation[13-15], surface doping[16-17], ligand modification[18-20], interface engineering[21-24].

One attractive multicomponent strategy is to break down the multiple reaction steps of CO_2-to-C_{2+} to have optimized components perform each step. In recent years, this "tandem catalysis" strategy has been successfully demonstrated in thermal heterogeneous catalysis[25-27]. Since it has been widely accepted that *CO (* denotes surface adsorbed species) and CO related intermediates are critical for CO_2RR towards multicarbons[4, 28-29], the tandem strategy is also suitable for CO_2 electrolysis. Due to excellent CO formation ability over Ag and Au, Cu-based bimetallic tandem platforms have been invoked for CO_2RR[30-34]. However, the practicality of such a strategy at high production rates (*i.e.* > 200 mA/cm^2) is still in question, due to CO_2 mass transport limitations in previous works. The gas diffusion electrode (GDE) can eliminate sluggish feed gas transportation kinetics by constructing an efficient three phase interface[35-36]. Nevertheless, the micro-environment around the catalyst may be considerably different during high-rate electrolysis compared with aqueous conditions[37]. Thus, to establish decoupled electrocatalytic CO_2-to-C_{2+} paradigms in high-rate electrochemical environments, the efficacy of a tandem platform should be evaluated in a gas diffusion electrode flow cell.

Here, in order to evaluate whether a tandem strategy can be utilized in high-rate CO_2 reduction, we designed a model two-component catalytic architecture in alkaline electrolyte with commercial Cu and Ag powder (Fig. 1a). Ag is selected for its high activity for CO formation during CO_2RR[38] and its thermodynamically immiscible nature with Cu at room temperature, thereby deconvolving enhancement due to bulk elemental alloying[39]. Although 1M KOH electrolyte is ultimately unsustainable for long term practical electrolysis due to electrolyte instability from reaction with CO_2, it is useful as a model environment to evaluate catalytic concepts at the early stage[37]. Compared against Cu alone, a significant enhancement of the partial current towards C_{2+} products (C_2H_4, C_2H_5OH, CH_3COOH) is observed over the tandem catalyst during CO_2 electrolysis, with a concurrent selectivity shift towards oxygenates over C_2H_4. Both post-electrolysis characterization and electrochemical CORR results confirm that the active sites over Ag and Cu surface work independently during CO_2RR, supporting the importance of a CO-rich local environment generated by the Ag component for enhancing C-C coupling on the Cu component in accordance with the tandem strategy. Furthermore, the normalized intrinsic activity towards C_{2+} products indicate that the Ag-generated microenvironment in tandem CO_2RR is superior to both pure CO_2 and CO atmosphere for Cu-catalyzed multicarbon production. This phenomenon suggests the existence of mechanisms for CO_2 reduction enhancement specifically stemming from tandem strategies and their resulting chemical microenvironments.

2. Results

2.1 Electrode characterization. A Cu-Ag tandem architecture catalyst was prepared by physical mixture of Cu and Ag nanopowders on carbon paper support and utilized in gas diffusion flow cells (Fig. S1) for high current CO_2 electrolysis. The morphology of commercial Cu and Ag powders is revealed with TEM (Fig. S2), showing that the crystalline feature size of both Cu and Ag is tens of nanometers, but heavily agglomerated with no distinct morphology. The electrode fabricated with these metal powders was name as Cu_xAg_y, representing a Cu-Ag tandem catalyst with x μg/cm^2 Cu and y μg/cm^2 Ag respectively (see experimental procedures). Then, these electrodes were imaged under SEM. The thickness of the catalyst layer in the as-prepared $Cu_{500}Ag_{1000}$ catalyst on carbon paper is several microns (Fig. 1b, 1c). SEM after electrolysis shows no significant structural change on the micron scale from the initial structure (Fig. S3).

Elemental characterization through XRD, XPS and EDS mapping (Fig. 1d, 1e, S4) provide further insight into the nature of the tandem catalyst. Both XRD patterns and XPS spectra of the as-prepared tandem $Cu_{500}Ag_{1000}$ catalyst show characteristic Cu and Ag related peaks without any observable peak shifting. Although the Cu LMM Auger peak indicates that the surface of nano powder has been oxidized, numerous studies[40-44] indicate that such a naturally formed oxide shell can be quickly reduced under working condition. Despite the ongoing debate in the community towards the existence and function of oxygen residue during CO_2RR[45-47], we note that such a phenomenon will not influence the conclusions related to tandem interactions between Ag and Cu of the later discussion in this work. Meanwhile, it is widely reported that Cu can undergo surface reconstruction and structural evolution during CO_2 electrolysis,[48-51] and previous reports have also invoked Cu-Ag alloy[13-15] or surface alloy[16] strategies to im-

prove CO_2RR catalytic performance. Thus, we conducted post-electrolysis characterization of the tandem $Cu_{500}Ag_{1000}$ catalyst to determine whether the structure is maintained. Previous works have shown structural and electronic differences owing to strong Ag interactions with Cu: for example, up to 0.8° Cu(111) peak shift in XRD could be found for a Cu-Ag alloy system[14] whereas up to 0.3 eV Cu $2p_{3/2}$ peak shift in XPS was reported for a Cu-Ag dimer.[23] In contrast, no peak shift of Cu or Ag could be observed for the tandem $Cu_{500}Ag_{1000}$ catalyst in either XRD, XPS or Cu LMM Auger peak after electrolysis, indicating the structural maintenance of this tandem catalyst and absence of electronic interactions between Ag and Cu throughout electrolysis. This absence is likely due to the bulk-like nature of Ag and Cu used, in addition to the mild conditions in which the electrode is fabricated, resulting in thermodynamically favored separation[52]. Importantly, this does not preclude the Ag-Cu surface and interfacial alloying observed in other reports which use more energetic fabrication conditions.

2.2 Enhanced CO_2RR catalytic performances toward C_{2+} products over tandem Cu-Ag catalysts. The polarization response curve of $Cu_{500}Ag_{1000}$ in Fig.2a shows higher geometric current density than Cu_{500} or Ag_{1000} alone under the same potentials. Interestingly, partial current densities toward C_{2+} products over different catalysts are also observed to be substantially higher for $Cu_{500}Ag_{1000}$, which cannot be explained simply through the individual contributions of Cu_{500} and Ag_{1000} (Fig. 2b). Explicitly, Ag_{1000} does not contribute to C-C coupling reactions in the potential range from -0.5 V to -0.8 V vs RHE. Thus, all partial current toward C_{2+} products should come from the Cu surface. Based on linear interpolation, the partial current toward C_{2+} products over Cu_{500} surface is only about 37 mA/cm^2 at -0.70V, while the corresponding C_{2+} partial current density over $Cu_{500}Ag_{1000}$ is 160 mA/cm^2. As the theoretical Cu loading density is constant between Cu_{500} and $Cu_{500}Ag_{1000}$, the significant enhancement of the C_{2+} partial current density over the tandem catalyst beginning at around -0.55 V vs RHE should be attributed to the additionally loaded Ag. The enhancement of C_{2+} products is shown to be dependent on the extent of Ag loading (Fig. S5), further reinforcing that Ag is responsible for the increase in C_{2+} production.

C_{2+} partial currents are further broken down to their main constituents to analyze how the tandem strategy influences product distribution (Fig.2c). Here we define the enhancement factor (EF) as the tandem $Cu_{500}Ag_{1000}$ partial current divided by that of the Cu_{500} catalyst alone. Beginning from -0.55 V vs RHE, the EFs of C_2H_4, C_2H_5OH and CH_3COO^- all increase significantly when the applied potential is more negative (Fig. 2c). Thus, relatively negative potential is essential to trigger the Ag-derived C_{2+} enhancement, achieving up to 6.43, 11.27, and 16.22 μg/h·cm$^2_{geom}$ production rates toward C_2H_4, C_2H_5OH and CH_3COO^- respectively over the Cu surface. Furthermore, oxygenate products are favored over C_2H_4 on the tandem catalyst, consistent with previous reports that invoke enhancement by local CO concentration [31, 51]. At -0.70 V vs RHE, the EFs are mostly at the same range as -0.65 V vs RHE, indicating that the tandem strategy induced enhancement is limited by factors beyond potential, such as the concentration of CO local to the catalyst. Similar trends can also be observed from tandem catalyst with other Cu-Ag ratios (Fig. S6).

To further probe the role of local CO towards the C_{2+} enhancement, the net CO producing abilities over these catalysts are also compared (Fig.2d). At potentials negative of -0.5 V vs. RHE, the C-C coupling reaction dominates such that net CO production rate over Cu_{500} remains at a relatively low level within the potential range. Meanwhile, Ag exhibits an exponential increase of CO production with respect to overpotential. Notably, the onset potential for C_{2+} enhancement is around -0.55 V vs RHE, where CO partial current on the pure Ag_{1000} catalyst is observed to take off. This indicates a direct correlation between C_{2+} enhancement on the $Cu_{500}Ag_{1000}$ catalyst and net CO production rate. Hence, the partial C_{2+} current enhancement is attributed to the high local CO created on the Ag surface within the tandem catalyst layer. Interestingly, Clark et al. invoked that the enhanced oxygenates selectivity is not attributed to localized CO produced by Ag, but by strain effects induced by surface Ag doping which modulates C-C coupling activity and suppresses HER.[16] Similarly, such HER suppression and oxygenates favoring phenomenon were also observed in other Cu-Ag alloy catalysts[14-15]. The differing contributions of tandem effects on catalysis (*i.e.* whether localized CO may influence further C_{2+} activity) between this work and previous works mentioned above may be due to the difference in electrolyte. It has been reported that high pH electrolyte can significantly accelerate C-C coupling reaction over Cu surface[36], which would correspond to more efficient utilization of CO in our system. Notably, the correlated suppression of HER typically observed from Ag-alloying or doping is not found in our system (Fig. S7), suggesting that the Ag doping effect is mostly negligible here and that the intrinsic catalytic activity of Cu is not influenced by Ag atomic interactions. More contextualization and comparison of relevant works can be found in Fig. S8 and Table S1.

2.3 Active site analysis and performance comparison based on CORR. Considering the importance of localized CO produced by the Cu-Ag tandem platform toward high rate C_{2+} chemicals production, we next investigated how such platforms behave under CO reduction reaction (CORR) conditions. If the addition of Ag electronically influences Cu active sites, we expect that CO reduction activity should differ between Cu and Cu-Ag catalysts[53]. However, in stark contrast to our previous observations in CO_2RR, the $Cu_{500}Ag_{1000}$ catalyst exhibits neither an enhancement in total current nor an enhancement in C_{2+} formation under CO-reducing conditions (Fig. 3a, 3b, S9). Thus, in both $Cu_{500}Ag_{1000}$ and Cu_{500} catalysts, only the Cu component conducts CORR. Meanwhile, no substantial enhancement is observed owing to the bimetallic platform in CORR across all multicarbon products, as shown explicitly in Fig. 3c, suggesting that the $Cu_{500}Ag_{1000}$ catalyst has no intrinsic enhancement in CO coupling compared with Cu_{500} alone.

In general, our CORR experiments strongly support the conclusion that Cu and Ag active sites operate independently. Ag produces CO from CO_2 and this generated CO in addition to the CO generated on Cu itself, is further utilized for multicarbon production over the Cu surface. In other words, we posit that in accordance with our structural characterization, Ag does not modify the Cu surface during tandem CO_2RR. We note that although electrocatalytic activity changes over longer periods of electrolysis, this is due to commonly reported stability issues with flooding in carbon paper based gas diffusion electrodes[36, 54-56], rather than to structural changes of the catalyst (Fig. S10). Moreover, given the similar activity between Cu and Cu-Ag catalysts in CORR when catalyst preparation is simply normalized by Cu mass loading, we further hypothesize that intrinsic catalytic activity towards multicarbons can be internally compared using Cu mass normalization.

2.4 Intrinsic catalytic performances of Cu catalyst under different local environments. Considering the production rate normalized by the mass of Cu as a measure of intrinsic catalyst activity for internal comparison, we sought to determine how the local gas environments would influence C_{2+} partial current over Cu surface (Fig. S11). Unsurprisingly, for CORR the activity towards all three main C_{2+} products over Cu_{500} are larger than for CO_2RR. However, we also observed unexpectedly that the normalized C_{2+} partial current over tandem $Cu_{500}Ag_{1000}$ during CO_2RR is beyond that of Cu_{500} during CORR. To exclude the influence of electron transfer differences in CO_2RR and CORR (*e.g.* for C_2H_4, $12e^-$ during CO2RR and $8e^-$ during CORR), we used the normalized intrinsic activity (in moles product per mass catalyst per time) to better represent the intrinsic performance over the Cu surface (Fig.4a-c). The normalized intrinsic activities of tandem $Cu_{500}Ag_{1000}$ towards C_2H_4, C_2H_5OH, $CH3COO^-$ in CO_2RR are 3~6-fold larger than that of Cu_{500} in CO_2RR at -0.7 V vs RHE. Moreover, the normalized intrinsic activities of tandem CO_2RR towards C_2H_4 and C_2H_5OH are still substantially larger than that of Cu_{500} in CORR(Fig.4d), such that the local environment created by the tandem catalyst favors a greater overall formation for C_{2+} than CORR on Cu alone. Given that the role of Ag is to supply Cu with a CO-rich local environment, we considered how a similar amount of Cu in place of Ag would behave. The normalized catalytic activity over $Cu_{500}Cu_{1000}$ is considerably lower than that of $Cu_{500}Ag_{1000}$, likely due to the deficient CO_2-to-CO activity of a Cu surface per surface site. (Fig. S12). Such results highlight the unexpected superiority of the tandem strategy for CO_2RR in a flow cell, which offers the opportunity to enhance the efficiency of C-C bonding on a Cu surface beyond conventional CORR during high-rate electrolysis.

The underlying mechanism accounting for this change in product distribution is also of interest. We find that the tandem-derived C_{2+} intrinsic activity enhancements over a Cu_{500} surface can also be imitated with a blended gas of 2% CO and 98% CO_2 (Fig. S13). Therefore, a mechanistic difference in mixed CO_2-CO atmosphere in the tandem catalyst layer may contribute to the enhancement of intrinsic activity towards a series of multicarbon products, similar to Strasser and co-workers' results in bicarbonate at lower electrolysis rates[57]. Other factors in the double layer may also be involved. For example, a relatively low CO coverage over Cu surface (2.5%~10% atm) can promote C_2H_4 formation rate during CORR[58] while *H coverage would influence C_2H_5OH formation during CO_2RR[59] by adsorbate-adsorbate interaction. Furthermore, the surface pH may also be an important influencing factor, due to subtle differences in the double layer given the presence of carbonate formation during CO_2RR[36]. With many possible mechanisms for the enhancement observed under tandem Cu-Ag CO_2RR conditions, Cu catalysts with well-defined surfaces as well as advanced *in-situ* spectroscopy techniques for flow cells will be valuable future mechanistic tools.

3. Discussion

In this work, we established and evaluated a Cu-Ag tandem platform for achieving high current CO_2 electrolysis towards C_{2+} products in a flow cell. In contrast with previous Cu-Ag works, Cu and Ag were confirmed to work independently in this system through post-electrolysis characterization and control experiments with CO reduction, such that the localized CO produced by Ag, with subsequent C-C bonding on Cu, is key towards high rate C_{2+} production. Furthermore, we found over the same Cu surface, the turnover of C_2H_4 and C_2H_5OH in a tandem CO_2-reducing platform is substantially higher than the activity for Cu in either pure CO_2 or pure CO-reducing conditions. Thus, we posit that the local environment created in high-rate tandem CO_2 electrolysis offers new opportunities for expanding the catalytic space of CO_2 electroreduction. Deep investigation of local CO atmosphere *in situ* is required to further understand high-rate tandem CO_2 electrolysis.

Moreover, we emphasize that although a highly alkaline electrolyte is beneficial for new catalytic architecture exploration and demonstration, serious concerns remain regarding its sustainability and stability issues due to the reaction between KOH and CO_2[37]. This may partially account for the lack of long-term stability observed in this work (Fig. S10). Translating the catalytic concept demonstrated here to truly practical CO_2 electrolysis requires systematic design that reduces CO_2 interaction with alkaline electrolyte while ideally still leveraging the catalytic benefits of local hydroxide. One avenue of interest may be to substitute bulk KOH electrolyte with local metal hydroxide at the cathode. Further exploration of catalyst design with cell engineering as a multi-scale strategy in sustainable electrolytes will undoubtedly be needed to enable practical tandem CO_2 electrolysis systems.

Experimental procedures

Resource Availability

Lead Contact

Further information and reasonable requests for resources and materials should be directed to and fulfilled by the Lead Contact, Peidong Yang (p_yang@berkeley.edu)

Materials Availability

All chemicals were purchased from commercial resources and used as received.

Data and Code Availability

There is no dataset or code associated with this work.

Materials

Commercial Cu powder (40-60 nm particle size (SAXS)), commercial Ag powder (<100 nm particle size), deuterium oxide (D_2O, 99.9 atom % D), dimethyl sulfoxide (DMSO, ACS reagent, ≥99.9%) and Nafion 117 ionomer solution (~5% in water and alcohol mixture) was purchased from Sigma-Aldrich. KOH pellets (>85%) were purchased from Fisher Chemicals. Anion exchange membrane (Fumasep FAA-3-PK-130) and Sigracet carbon papers were ordered from Fuel Cell Store. Ag/AgCl (3M KCl) reference electrodes were purchased from CH Instrument. Platinum gauze (99.9% metal basis) was purchased from Alfa Aesar. Carbon dioxide (CO2, 4.5LS), carbon monoxide (4.0 research) and Argon gas were purchased from Praxair. Deionized water (DI water with 18.2 MΩ·cm, <5 ppb TOC) was obtained from a Millipore water system.

Electrode preparations

The following procedures describe the fabrication of a $Cu_{500}Ag_{1000}$ catalyst, with other catalysts produced in a similar fashion and adjusting for mass. 12 mg commercial Cu or Ag nano-powder was firstly mixed with 4 ml ethanol, 40 μl Nafion ionomer solution and then sonicated for 1h in the water bath to produce a uniform ink. Cu and Ag inks were mixed together with 1:2 volume ratio and then spray-cast on carbon paper with a spray gun (SPEEDAIRE, Mod. 48PX90). After that, the fabricated electrode was stored in a vacuum desiccator overnight to remove residual ethanol. $Cu_{500}Ag_{1000}$ represents a Cu-Ag tandem catalyst with 500 μg/cm^2 Cu and 1000 μg/cm^2 Ag theoretically. The weight difference of carbon paper before and after spraying was measured by an analytical balance to confirm the loading amount.

Characterization

The image of Cu and Ag powder morphology was collected by a transmission electron microscopy (Tecnai G2 T20 S-TWIN) under 200 kV. Scanning Electron Microscopy (Ultra 55-FESEM) is operated at 5 keV with 5 mm working distance to characterize the fabricated electrode morphology and elemental distribution before and after electrolysis. XRD (Bruker D8) patterns were collected using a Cu target. X-ray photoelectron spectroscopy (XPS) (Thermo Scientific K-Alpha) measurement was conducted using an Al Kα source. For all post-electrolysis samples, electrodes were taken after CO_2 electrolysis at 200 mA/cm^2 constant current density for 30 min, then rinsed with deionized water and isopropanol repeatedly in order to remove as much electrolyte residue as possible and dried in a vacuum desiccator before measurement.

Electrochemical experiments and products characterization

All CO_2 and CO involved electrolysis were conducted in a gas diffusion flow cell. Before electrolysis, electrolyte was firstly bubbled with argon for at least 30 min to remove dissolved oxygen. In this work, 1 M KOH was used as the electrolyte. The gas flow rate during electrolysis was controlled by a mass flow controller at 25 sccm while the electrolyte flow rates in cathode and anode channels were managed by two low-flow chemical metering pumps at 5 ml/min. The flow-out electrolyte would be directly collected for product analysis or transferred to waste bottle instead of feeding back to the cell in order to eliminate pH drop induced by neutralization reaction between KOH and CO_2. During all electrolysis, the cathode and anode were separated by a Fumasep anion exchange membrane. Ag/AgCl (3M KCl) was used as reference electrode. Considering batch to batch difference and harsh working conditions (high current and high pH), the Ag/AgCl reference electrode was frequently calibrated and replaced if needed.

During chronopotentiometry (CP), both gas and liquid products were collected and analyzed. Sampling was conducted at least 300 s after the electrolysis began in order to let the system reach steady state. No automatic iR correction was applied during CP experiments. After product collection, the cathodic potential and resistance between working electrode and reference electrode

were precisely measured by a subsequent current interrupt (CI) experiment. The back-calculated potentials were based on the following equation:

$$E_{\text{vs RHE}} = E_{\text{vs Ag/AgCl}} + iR + E_{\text{Ag/AgCl vs RHE}}$$

The RHE potential is calculated using a pH value of 14. After electrolysis, gas products, including CO, CH_4, C_2H_4 and H_2 were detected and quantified using gas chromatography (Agilent 7890B GC system). Three GC columns (1.5 ft HayeSep Q, 6 ft HayeSep Q and 6 ft Molsieve 5A) are used to separate different gases. CO and CO_2 were additionally transformed into CH_4 with a methanizer. H_2 was detected by TCD (Ar flow) while other gases were detected by FID. Liquid products were analyzed by 1H nuclear magnetic resonance (Bruker AV600 with a 5 mm Z-gradient triple resonance 1H/BB Prodigy cryo-probe) with water suppression by excitation sculpting. DMSO was used as an internal standard for quantitative NMR. Through the calibration curve, the concentration of the products can be determined (unit: mM for liquid products and ppm for gas products). Partial current density of the products can be calculated with the following equations:

$$j_{\text{gas product}} = c_{\text{gas product}} \times 10^{-5} \times e^{-} \text{ transfer number} \times F \times v_{\text{gas}} / (V_m \times S)$$

and

$$j_{\text{liquid product}} = c_{\text{liquid product}} \times e^{-} \text{ transfer number} \times F \times v_{\text{electrolyte}} / S$$

where：

j: partial current density (mA/cm^2)

c: concentration of the product in gas phase (ppm) or electrolyte (M)

F: Faraday constant (96485 C/mol)

v: flow rate (mL/s)

V_m: molar volume at room temperature and pressure (293 K, 1 atm)

S: electrode geometric area (cm^2)

Subsequently, faraday efficiency (FE) can be obtained with:

$$FE = j_{\text{product}} / j_{\text{total}} \times 100\%$$

Specifically, in this work, enhancement factor (EF) at specific potentials was defined as:

$$EF = j_{\text{product on tandem catalyst}} / j_{\text{product on single Cu catalyst}}$$

And normalized intrinsic activity towards multicarbons was calculated with following equation:

$$\text{normalized intrinsic activity} = j_{\text{product}} / (F \times e^{-} \text{ transfer number} \times d_{Cu})$$

where:

d_{Cu}: Cu loading density (mg/cm^2)

Acknowledgment

This work was supported by Director, Office of Science, Office of Basic Energy Sciences, Chemical Sciences, Geosciences, & Biosciences Division, of the US Department of Energy under Contract DE-AC02- 05CH11231, FWP CH030201 (Catalysis Research Program). We thank Prof. Edward H. Sargent for their sharing of the gas diffusion cell design and Prof. Cao-Thang Dinh for initial calibration samples. Trans-

mission electron microscopy was conducted with help from Prof. Paul Alivisatos group. Scanning electron microscopy, and X-ray photoelectron spectroscopy were conducted using facilities at the Molecular Foundry. Work at the Molecular Foundry was supported by the Office of Science, Office of Basic Energy Sciences, of the U.S. Department of Energy under Contract No. DE-AC02-05CH11231. We thank Dr. Hasan Celik and UC Berkeley's NMR facility in the College of Chemistry (CoC-NMR) for spectroscopic assistance. Instruments in the CoC-NMR are supported in part by NIH S10OD024998. C.C. and J.J. gratefully acknowledge the support from Suzhou Industrial Park Scholarship. S.Y. acknowledges support from Samsung Scholarship. M.B.R. acknowledges support from the CIFAR Bio-Inspired Solar Energy Postdoctoral Fellowship.

Author Contributions

C.C. designed the systems, collected and analyzed data, and wrote the manuscript. Y.L., J.J and M.L. analyzed data and wrote the manuscript. S.Y. and S.L. collected data. M.B.R. contributed to system setup. P.Y. designed the systems, analyzed data, and wrote the manuscript.

Declaration of Interests

The authors declare no competing financial interest.

References

(1) Kibria, M. G.; Edwards, J. P.; Gabardo, C. M.; Dinh, C. T.; Seifitokaldani, A.; Sinton, D. and Sargent, E. H., (2019). Electrochemical CO2 Reduction into Chemical Feedstocks: From Mechanistic Electrocatalysis Models to System Design. Adv. Mater. *31*, 1807166.
(2) Seh, Z. W.; Kibsgaard, J.; Dickens, C. F.; Chorkendorff, I.; Norskov, J. K. and Jaramillo, T. F., (2017). Combining theory and experiment in electrocatalysis: Insights into materials design. Science *355*, eaad4998.
(3) Bushuyev, O. S.; De Luna, P.; Dinh, C. T.; Tao, L.; Saur, G.; van de Lagemaat, J.; Kelley, S. O. and Sargent, E. H., (2018). What Should We Make with CO 2 and How Can We Make It? Joule *2*, 825-832.
(4) Ross, M. B.; De Luna, P.; Li, Y.; Dinh, C.-T.; Kim, D.; Yang, P. and Sargent, E. H., (2019). Designing materials for electrochemical carbon dioxide recycling. Nat. Catal. *2*, 648-658.
(5) Ross, M. B.; Li, Y.; De Luna, P.; Kim, D.; Sargent, E. H. and Yang, P., (2019). Electrocatalytic Rate Alignment Enhances Syngas Generation. Joule *3*, 257-264.
(6) Li, T.; Lees, E. W.; Goldman, M.; Salvatore, D. A.; Weekes, D. M. and Berlinguette, C. P., (2019). Electrolytic Conversion of Bicarbonate into CO in a Flow Cell. Joule *3*, 1487-1497.
(7) Ren, S.; Joulié, D.; Salvatore, D.; Torbensen, K.; Wang, M.; Robert, M. and Berlinguette, C. P., (2019). Molecular electrocatalysts can mediate fast, selective CO2 reduction in a flow cell. Science *365*, 367-369.
(8) Gu, J.; Hsu, C.-S.; Bai, L.; Chen, H. M. and Hu, X., (2019). Atomically dispersed Fe3+ sites catalyze efficient CO2 electroreduction to CO. Science *364*, 1091-1094.
(9) Liu, M.; Pang, Y.; Zhang, B.; De Luna, P.; Voznyy, O.; Xu, J.; Zheng, X.; Dinh, C. T.; Fan, F.; Cao, C.; de Arquer, F. P.; Safaei, T. S.; Mepham, A.; Klinkova, A.; Kumacheva, E.; Filleter, T.; Sinton, D.; Kelley, S. O. and Sargent, E. H., (2016). Enhanced electrocatalytic CO2 reduction via field-induced reagent concentration. Nature *537*, 382-386.
(10) Hori, Y.; Murata, A. and Takahashi, R., (1989). Formation of hydrocarbons in the electrochemical reduction of carbon dioxide at a copper electrode in aqueous solution. J. Chem. Soc., Faraday Trans. 1 *85*, 2309-2326.
(11) Garza, A. J.; Bell, A. T. and Head-Gordon, M., (2018). Mechanism of CO2 Reduction at Copper Surfaces: Pathways to C2 Products. ACS catal. *8*, 1490-1499.
(12) Ma, M.; Djanashvili, K. and Smith, W. A., (2016). Controllable hydrocarbon formation from the electrochemical reduction of CO2 over Cu nanowire arrays. Angew. Chem. Int. Ed. *55*, 6680-6684.
(13) Hoang, T. T. H.; Verma, S.; Ma, S.; Fister, T. T.; Timoshenko, J.; Frenkel, A. I.; Kenis, P. J. A. and Gewirth, A. A., (2018). Nanoporous Copper-Silver Alloys by Additive-Controlled Electrodeposition for the Selective Electroreduction of CO2 to Ethylene and Ethanol. J. Am. Chem. Soc. *140*, 5791-5797.
(14) Li, Y. C.; Wang, Z.; Yuan, T.; Nam, D. H.; Luo, M.; Wicks, J.; Chen, B.; Li, J.; Li, F.; de Arquer, F. P. G.; Wang, Y.; Dinh, C. T.; Voznyy, O.; Sinton, D. and Sargent, E. H., (2019). Binding Site Diversity Promotes CO2 Electroreduction to Ethanol. J. Am. Chem. Soc. *141*, 8584-8591.
(15) Lee, S.; Park, G. and Lee, J., (2017). Importance of Ag–Cu biphasic boundaries for selective electrochemical reduction of CO2 to ethanol. ACS catal. *7*, 8594-8604.
(16) Clark, E. L.; Hahn, C.; Jaramillo, T. F. and Bell, A. T., (2017). Electrochemical CO2 Reduction over Compressively Strained CuAg Surface Alloys with Enhanced Multi-Carbon Oxygenate Selectivity. J. Am. Chem. Soc. *139*, 15848-15857.
(17) Zhou, Y.; Che, F.; Liu, M.; Zou, C.; Liang, Z.; De Luna, P.; Yuan, H.; Li, J.; Wang, Z.; Xie, H.; Li, H.; Chen, P.; Bladt, E.; Quintero-Bermudez, R.; Sham, T. K.; Bals, S.; Hofkens, J.; Sinton, D.; Chen, G. and Sargent, E. H., (2018). Dopant-induced electron localization drives CO2 reduction to C2 hydrocarbons. Nat. Chem. *10*, 974-980.
(18) Buckley, A. K.; Lee, M.; Cheng, T.; Kazantsev, R. V.; Larson, D. M.; Goddard Iii, W. A.; Toste, F. D. and Toma, F. M., (2019). Electrocatalysis at Organic-Metal Interfaces: Identification of Structure-Reactivity Relationships for CO2 Reduction at Modified Cu Surfaces. J. Am. Chem. Soc. *141*, 7355-7364.
(19) Hoang, T. T. H.; Ma, S.; Gold, J. I.; Kenis, P. J. A. and Gewirth, A. A., (2017). Nanoporous Copper Films by Additive-Controlled Electrodeposition: CO2 Reduction Catalysis. ACS catal. *7*, 3313-3321.
(20) Han, Z.; Kortlever, R.; Chen, H. Y.; Peters, J. C. and Agapie, T., (2017). CO2 Reduction Selective for C>/=2 Products on Polycrystalline Copper with N-Substituted Pyridinium Additives. ACS Cent. Sci. *3*, 853-859.
(21) Chang, X.; Wang, T.; Zhao, Z. J.; Yang, P.; Greeley, J.; Mu, R.; Zhang, G.; Gong, Z.; Luo, Z.; Chen, J.; Cui, Y.; Ozin, G. A. and Gong, J., (2018). Tuning Cu/Cu2 O Interfaces for the Reduction of Carbon Dioxide to Methanol in Aqueous Solutions. Angew. Chem. Int. Ed. *57*, 15415-15419.

(22) Bai, S.; Shao, Q.; Wang, P.; Dai, Q.; Wang, X. and Huang, X., (2017). Highly Active and Selective Hydrogenation of CO2 to Ethanol by Ordered Pd-Cu Nanoparticles. J. Am. Chem. Soc. *139*, 6827-6830.
(23) Huang, J.; Mensi, M.; Oveisi, E.; Mantella, V. and Buonsanti, R., (2019). Structural Sensitivities in Bimetallic Catalysts for Electrochemical CO2 Reduction Revealed by Ag-Cu Nanodimers. J. Am. Chem. Soc. *141*, 2490-2499.
(24) Varandili, S. B.; Huang, J.; Oveisi, E.; De Gregorio, G. L.; Mensi, M.; Strach, M.; Vavra, J.; Gadiyar, C.; Bhowmik, A. and Buonsanti, R., (2019). Synthesis of Cu/CeO2-x Nanocrystalline Heterodimers with Interfacial Active Sites To Promote CO2 Electroreduction. ACS catal. *9*, 5035-5046.
(25) Yamada, Y.; Tsung, C.-K.; Huang, W.; Huo, Z.; Habas, S. E.; Soejima, T.; Aliaga, C. E.; Somorjai, G. A. and Yang, P., (2011). Nanocrystal bilayer for tandem catalysis. Nat. Chem. *3*, 372-376.
(26) Xie, C.; Chen, C.; Yu, Y.; Su, J.; Li, Y.; Somorjai, G. A. and Yang, P., (2017). Tandem Catalysis for CO2 Hydrogenation to C2-C4 Hydrocarbons. Nano Lett. *17*, 3798-3802.
(27) Li, Z.; Qu, Y.; Wang, J.; Liu, H.; Li, M.; Miao, S. and Li, C., (2019). Highly selective conversion of carbon dioxide to aromatics over tandem catalysts. Joule *3*, 570-583.
(28) Nitopi, S.; Bertheussen, E.; Scott, S. B.; Liu, X.; Engstfeld, A. K.; Horch, S.; Seger, B.; Stephens, I. E. L.; Chan, K.; Hahn, C.; Norskov, J. K.; Jaramillo, T. F. and Chorkendorff, I., (2019). Progress and Perspectives of Electrochemical CO2 Reduction on Copper in Aqueous Electrolyte. Chem. Rev. *119*, 7610-7672.
(29) Li, F.; Li, Y. C.; Wang, Z.; Li, J.; Nam, D.-H.; Lum, Y.; Luo, M.; Wang, X.; Ozden, A.; Hung, S.-F.; Chen, B.; Wang, Y.; Wicks, J.; Xu, Y.; Li, Y.; Gabardo, C. M.; Dinh, C.-T.; Wang, Y.; Zhuang, T.-T.; Sinton, D. and Sargent, E. H., (2019). Cooperative CO2-to-ethanol conversion via enriched intermediates at molecule–metal catalyst interfaces. Nat. Catal. *3*, 75-82.
(30) Fu, J.; Zhu, W.; Chen, Y.; Yin, Z.; Li, Y.; Liu, J.; Zhang, H.; Zhu, J. and Sun, S., (2019). Bipyridine-assisted assembly of Au nanoparticles on Cu nanowires to enhance electrochemical reduction of CO2. Angew. Chem. Int. Ed. *58*, 14100-14103.
(31) Lum, Y. and Ager, J. W., (2018). Sequential catalysis controls selectivity in electrochemical CO2 reduction on Cu. Energy Environ. Sci. *11*, 2935-2944.
(32) Gurudayal, G.; Perone, D.; Malani, S.; Lum, Y.; Haussener, S. and Ager, J. W., (2019). Sequential Cascade Electrocatalytic Conversion of Carbon Dioxide to CC Coupled Products. ACS Appl. Energy Mater. *2*, 4551-4559.
(33) Morales-Guio, C. G.; Cave, E. R.; Nitopi, S. A.; Feaster, J. T.; Wang, L.; Kuhl, K. P.; Jackson, A.; Johnson, N. C.; Abram, D. N.; Hatsukade, T.; Hahn, C. and Jaramillo, T. F., (2018). Improved CO2 reduction activity towards C2+ alcohols on a tandem gold on copper electrocatalyst. Nat. Catal. *1*, 764-771.
(34) Gao, J.; Zhang, H.; Guo, X.; Luo, J.; Zakeeruddin, S. M.; Ren, D. and Grätzel, M., (2019). Selective C–C Coupling in Carbon Dioxide Electroreduction via Efficient Spillover of Intermediates As Supported by Operando Raman Spectroscopy. J. Am. Chem. Soc. *141*, 18704-18714.
(35) Li, J.; Chen, G.; Zhu, Y.; Liang, Z.; Pei, A.; Wu, C.-L.; Wang, H.; Lee, H. R.; Liu, K.; Chu, S. and Cui, Y., (2018). Efficient electrocatalytic CO2 reduction on a three-phase interface. Nat. Catal. *1*, 592-600.
(36) Dinh, C.-T.; Burdyny, T.; Kibria, M. G.; Seifitokaldani, A.; Gabardo, C. M.; de Arquer, F. P. G.; Kiani, A.; Edwards, J. P.; De Luna, P. and Bushuyev, O. S., (2018). CO2 electroreduction to ethylene via hydroxide-mediated copper catalysis at an abrupt interface. Science *360*, 783-787.
(37) Burdyny, T. and Smith, W. A., (2019). CO2 reduction on gas-diffusion electrodes and why catalytic performance must be assessed at commercially-relevant conditions. Energy Environ. Sci. *12*, 1442-1453.
(38) Zheng, T.; Jiang, K. and Wang, H., (2018). Recent Advances in Electrochemical CO2 -to-CO Conversion on Heterogeneous Catalysts. Adv. Mater. *3*, 1802066.
(39) Lee, C. W.; Yang, K. D.; Nam, D. H.; Jang, J. H.; Cho, N. H.; Im, S. W. and Nam, K. T., (2018). Defining a Materials Database for the Design of Copper Binary Alloy Catalysts for Electrochemical CO2 Conversion. Adv. Mater. *30*, 1704717.
(40) Zhuang, T.-T.; Pang, Y.; Liang, Z.-Q.; Wang, Z.; Li, Y.; Tan, C.-S.; Li, J.; Dinh, C. T.; De Luna, P.; Hsieh, P.-L.; Burdyny, T.; Li, H.-H.; Liu, M.; Wang, Y.; Li, F.; Proppe, A.; Johnston, A.; Nam, D.-H.; Wu, Z.-Y.; Zheng, Y.-R.; Ip, A. H.; Tan, H.; Chen, L.-J.; Yu, S.-H.; Kelley, S. O.; Sinton, D. and Sargent, E. H., (2018). Copper nanocavities confine intermediates for efficient electrosynthesis of C3 alcohol fuels from carbon monoxide. Nat. Catal. *1*, 946-951.
(41) Li, Y.; Kim, D.; Louisia, S.; Xie, C.; Kong, Q.; Yu, S.; Lin, T.; Aloni, S.; Fakra, S. C. and Yang, P., (2020). Electrochemically scrambled nanocrystals are catalytically active for CO2-to-multicarbons. Proc. Natl. Acad. Sci. U.S.A. *117*, 9194-9201.
(42) Farmand, M.; Landers, A. T.; Lin, J. C.; Feaster, J. T.; Beeman, J. W.; Ye, Y.; Clark, E. L.; Higgins, D.; Yano, J.; Davis, R. C.; Mehta, A.; Jaramillo, T. F.; Hahn, C. and Drisdell, W. S., (2019). Electrochemical flow cell enabling operando probing of electrocatalyst surfaces by X-ray spectroscopy and diffraction. Phys. Chem. Chem. Phys. *21*, 5402-5408.
(43) Arán-Ais, R. M.; Scholten, F.; Kunze, S.; Rizo, R. and Cuenya, B. R., (2020). The role of in situ generated morphological motifs and Cu (i) species in C 2+ product selectivity during CO 2 pulsed electroreduction. Nature Energy *5*, 317-325.
(44) Lum, Y. and Ager, J. W., (2018). Stability of Residual Oxides in Oxide-Derived Copper Catalysts for Electrochemical CO2 Reduction Investigated with (18) O Labeling. Angew. Chem. Int. Ed. *57*, 551-554.
(45) Gao, D.; Zegkinoglou, I.; Divins, N. J.; Scholten, F.; Sinev, I.; Grosse, P. and Roldan Cuenya, B., (2017). Plasma-Activated Copper Nanocube Catalysts for Efficient Carbon Dioxide Electroreduction to Hydrocarbons and Alcohols. ACS Nano *11*, 4825-4831.
(46) Jung, H.; Lee, S. Y.; Lee, C. W.; Cho, M. K.; Won, D. H.; Kim, C.; Oh, H. S.; Min, B. K. and Hwang, Y. J., (2019). Electrochemical fragmentation of Cu2O nanoparticles enhancing selective C-C coupling from CO2 reduction reaction. J. Am. Chem. Soc. *141*, 4624-4633.
(47) Chou, T. C.; Chang, C. C.; Yu, H. L.; Yu, W. Y.; Dong, C. L.; Velasco-Velez, J. J.; Chuang, C. H.; Chen, L. C.; Lee, J. F.; Chen, J. M. and Wu, H. L., (2020). Controlling the Oxidation State of the Cu Electrode and Reaction Intermediates for Electrochemical CO2 Reduction to Ethylene. J. Am. Chem. Soc. *142*, 2857-2867.
(48) Kim, D.; Kley, C. S.; Li, Y. and Yang, P., (2017). Copper nanoparticle ensembles for selective electroreduction of CO2 to C2–C3 products. Proc. Natl. Acad. Sci. U.S.A. *114*, 10560-10565.
(49) Huang, J.; Hormann, N.; Oveisi, E.; Loiudice, A.; De Gregorio, G. L.; Andreussi, O.; Marzari, N. and Buonsanti, R., (2018). Potential-induced nanoclustering of metallic catalysts during electrochemical CO2 reduction. Nat. Commun. *9*, 3117.
(50) Kim, Y. G.; Baricuatro, J. H.; Javier, A.; Gregoire, J. M. and Soriaga, M. P., (2014). The evolution of the polycrystalline copper surface, first to Cu(111) and then to Cu(100), at a fixed CO(2)RR potential: a study by operando EC-STM. Langmuir *30*, 15053-15056.
(51) Osowiecki, W. T.; Nussbaum, J. J.; Kamat, G. A.; Katsoukis, G.; Ledendecker, M.; Frei, H.; Bell, A. T. and Alivisatos, A. P., (2019). Factors and Dynamics of Cu Nanocrystal Reconstruction under CO2 Reduction. ACS Appl. Energy Mater. *2*, 7744-7749.
(52) Osowiecki, W. T.; Ye, X.; Satish, P.; Bustillo, K. C.; Clark, E. L. and Alivisatos, A. P., (2018). Tailoring Morphology of Cu-Ag Nanocrescents and Core-Shell Nanocrystals Guided by a Thermodynamic Model. J. Am. Chem. Soc.
(53) Wang, X.; Wang, Z.; Zhuang, T.-T.; Dinh, C.-T.; Li, J.; Nam, D.-H.; Li, F.; Huang, C.-W.; Tan, C.-S. and Chen, Z., (2019). Efficient upgrading of CO to C 3 fuel using asymmetric CC coupling active sites. Nat. Commun. *10*, 5186.
(54) Wang, Y.; Shen, H.; Livi, K. J.; Raciti, D.; Zong, H.; Gregg, J.; Onadeko, M.; Wan, Y.; Watson, A. and Wang, C., (2019). Copper Nanocubes for CO2 Reduction in Gas Diffusion Electrodes. Nano Lett. *19*, 8461-8468.

(55) Luc, W.; Fu, X.; Shi, J.; Lv, J.-J.; Jouny, M.; Ko, B. H.; Xu, Y.; Tu, Q.; Hu, X.; Wu, J.; Yue, Q.; Liu, Y.; Jiao, F. and Kang, Y., (2019). Two-dimensional copper nanosheets for electrochemical reduction of carbon monoxide to acetate. Nat. Catal. *2*, 423-430.
(56) Jouny, M.; Luc, W. and Jiao, F., (2018). High-rate electroreduction of carbon monoxide to multi-carbon products. Nat. Catal. *1*, 748-755.
(57) Wang, X.; de Araujo, J. F.; Ju, W.; Bagger, A.; Schmies, H.; Kuhl, S.; Rossmeisl, J. and Strasser, P., (2019). Mechanistic reaction pathways of enhanced ethylene yields during electroreduction of CO2-CO co-feeds on Cu and Cu-tandem electrocatalysts. Nat. Nanotechnol. *14*, 1063-1070.
(58) Li, J.; Wang, Z.; McCallum, C.; Xu, Y.; Li, F.; Wang, Y.; Gabardo, C. M.; Dinh, C.-T.; Zhuang, T.-T.; Wang, L.; Howe, J. Y.; Ren, Y.; Sargent, E. H. and Sinton, D., (2019). Constraining CO coverage on copper promotes high-efficiency ethylene electroproduction. Nat. Catal. *2*, 1124-1131.
(59) Luo, M.; Wang, Z.; Li, Y. C.; Li, J.; Li, F.; Lum, Y.; Nam, D. H.; Chen, B.; Wicks, J.; Xu, A.; Zhuang, T.; Leow, W. R.; Wang, X.; Dinh, C. T.; Wang, Y.; Wang, Y.; Sinton, D. and Sargent, E. H., (2019). Hydroxide promotes carbon dioxide electroreduction to ethanol on copper via tuning of adsorbed hydrogen. Nat. Commun. *10*, 5814.

Figure 1. **Cu-Ag tandem architecture design and characterizations**. (a) Scheme of the Cu-Ag tandem platform for high rate CO_2 electrolysis and C_{2+} products formation. (b) Top view SEM image of $Cu_{500}Ag_{1000}$ catalyst over carbon paper before electrolysis. (c) Cross-section SEM image of $Cu_{500}Ag_{1000}$ catalyst over carbon paper before electrolysis. (d) XRD patterns of $Cu_{500}Ag_{1000}$ catalyst over carbon paper before and after electrolysis. Inset: Cu(111) and Ag(200) range enlarged. Standard PDF index of Cu (ICDD PDF# 99-0034) and Ag (ICDD PDF# 99-0094) are plotted for comparison. (e) XPS spectrum of $Cu_{500}Ag_{1000}$ catalyst over carbon paper before and after electrolysis, with Cu_{500} and Ag_{1000} for comparison. Post-electrolysis samples were prepared after conducting CO_2RR at 200 mA/cm^2 constant cathodic current density for 30 min.

Figure 2. CO_2RR performance of tandem catalysts comparing with pure metal catalysts. (a) Total geometric current density curve of $Cu_{500}Ag_{1000,}$ Cu_{500} and Ag_{1000} catalysts. (b) Partial current density towards C_{2+} products over $Cu_{500}Ag_{1000,}$ Cu_{500} and Ag_{1000} catalysts. (c) Enhancement factors (EF) for total C_{2+} and individual products over four different potentials (-0.55V, -0.60V, -0.65V and -0.70V vs RHE) in CO_2RR, which is defined as the tandem $Cu_{500}Ag_{1000}$ partial current divided by that of Cu_{500} catalyst alone. Linear interpolation was used to obtain the estimated current values at these potentials. (d) CO production partial current density over $Cu_{500}Ag_{1000,}$ Cu_{500} and Ag_{1000} catalysts. Data points with error bars (1 SD) in all figures based on average value of three separate experiments results.

Figure 3. **CORR performance of tandem catalysts comparing with pure metal catalysts.** (a) Total currents of CO electroreduction reaction (CORR) over $Cu_{500}Ag_{1000}$, Cu_{500} and Ag_{1000} catalysts. (b) C_{2+} products partial currents of CORR over $Cu_{500}Ag_{1000}$ and Cu_{500} catalysts. (c) Enhancement factors (EF) for total C_{2+} and individual products over four different potentials (-0.62V, -0.66V, -0.70V and -0.74V vs RHE) in CORR, calculated as described in Figure 2.

Figure 4. Normalized intrinsic activity analysis and corresponding schematic illustration. Normalized intrinsic activity towards (a) C_2H_4 (b) C_2H_5OH (c) CH_3COO^- over the Cu surface with different local environments (tandem CO_2 in red, fed CO in yellow, and fed

CO_2 in blue). Data points with error bars (1 SD) in all figures based on average value of three separated experimental results. (d) Scheme representing the catalytic difference provided by the local environment produced by the tandem catalyst (red) vs. standard CORR (yellow) or CO_2RR (blue).

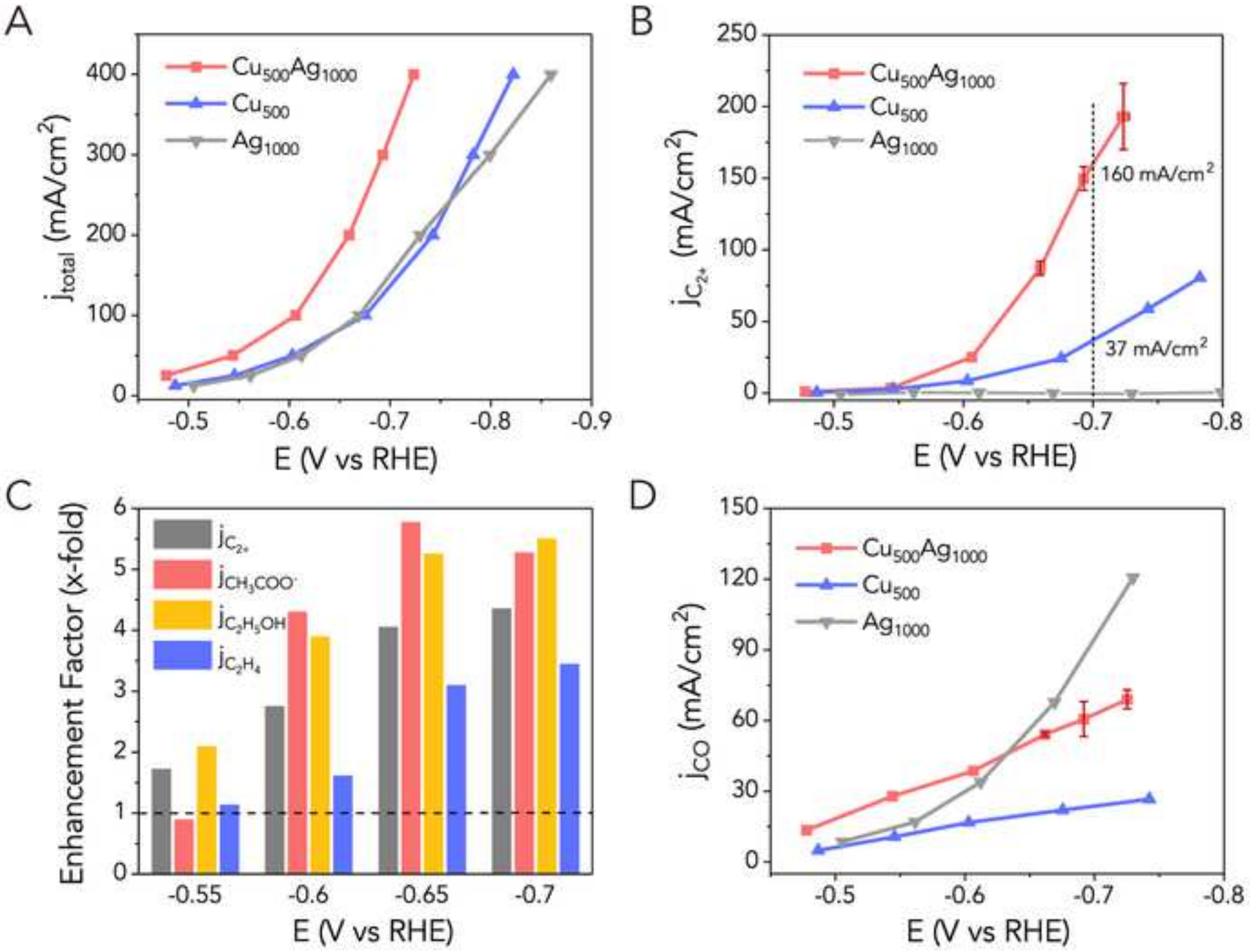

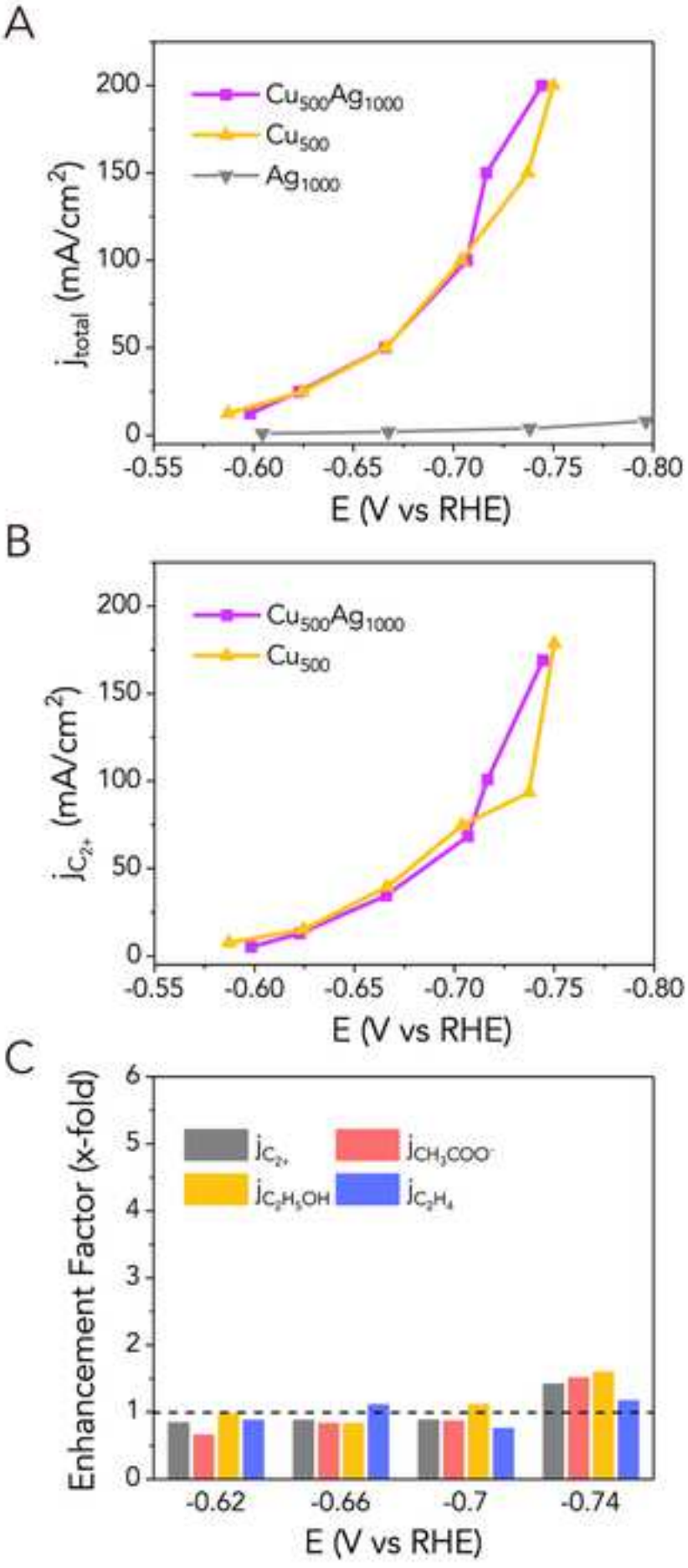

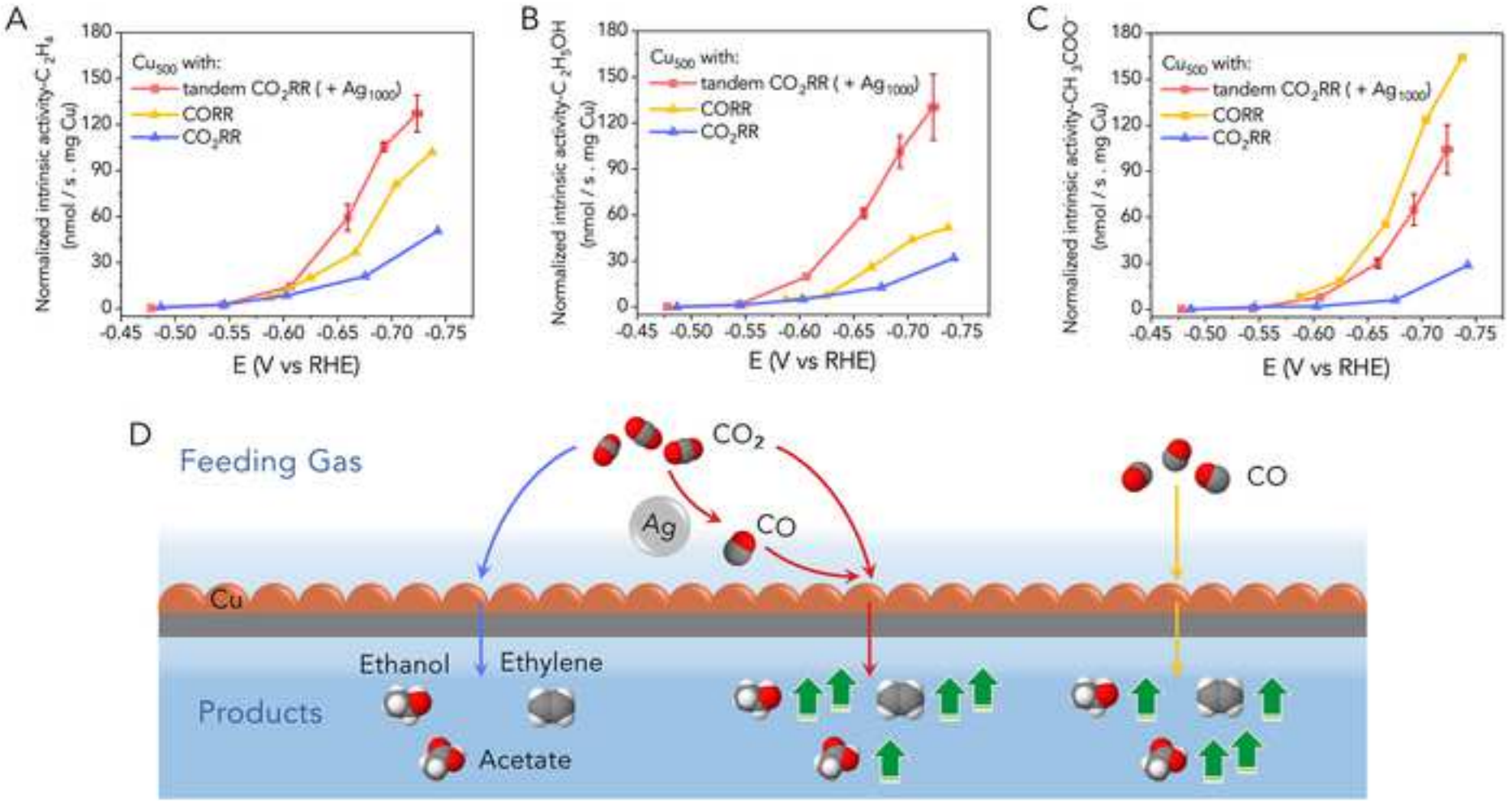

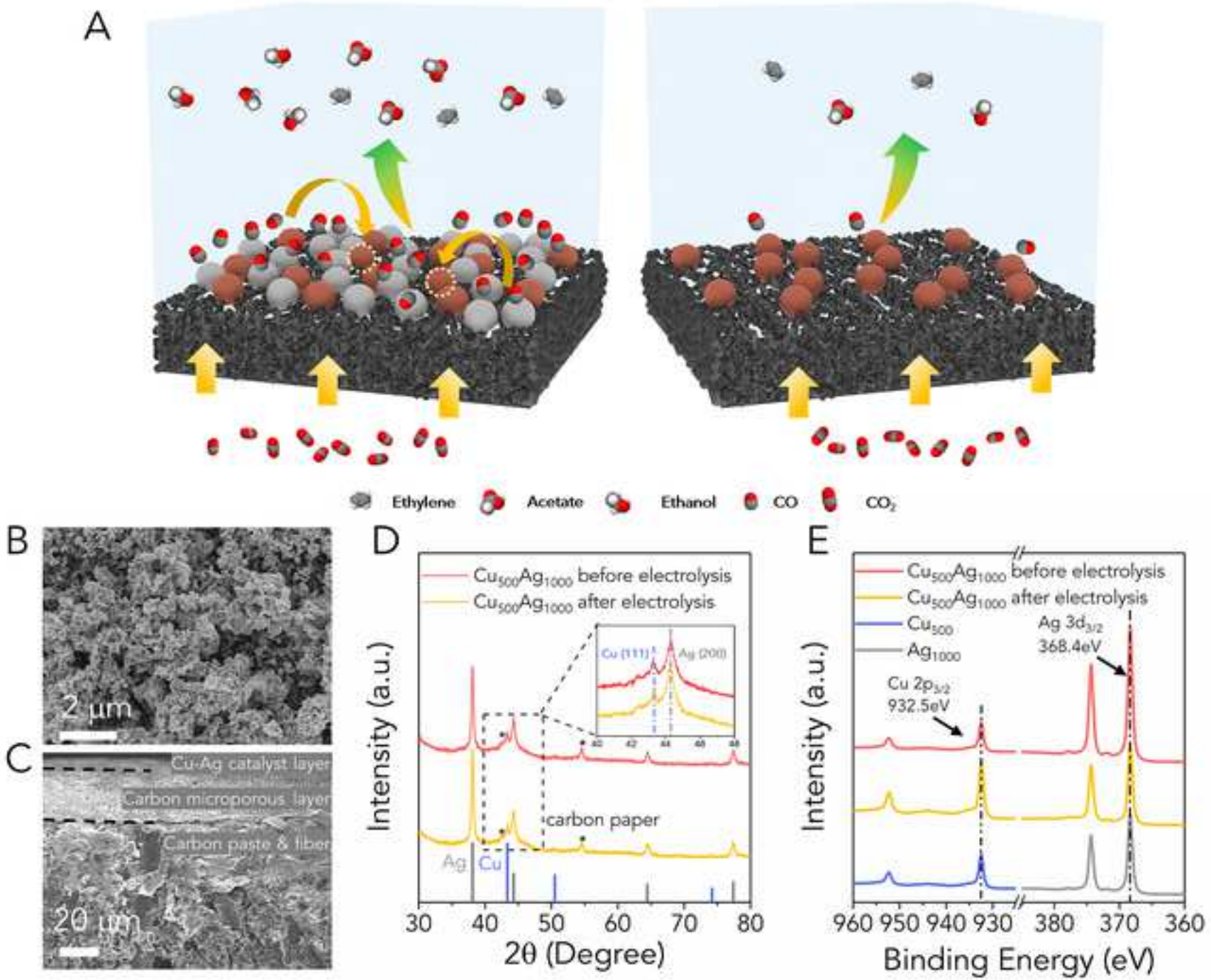

Content:

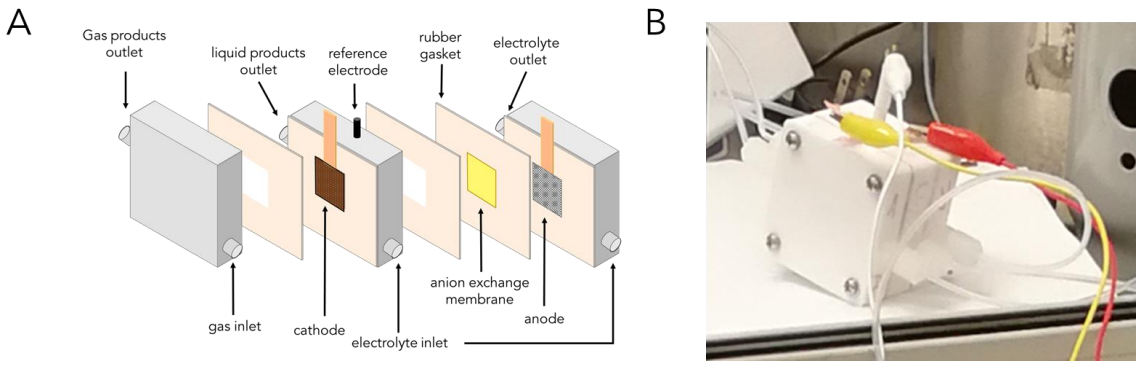

Figure S1. **Gas diffusion cell configuration used in this work:** (a) schematic illustration and (b) photograph.

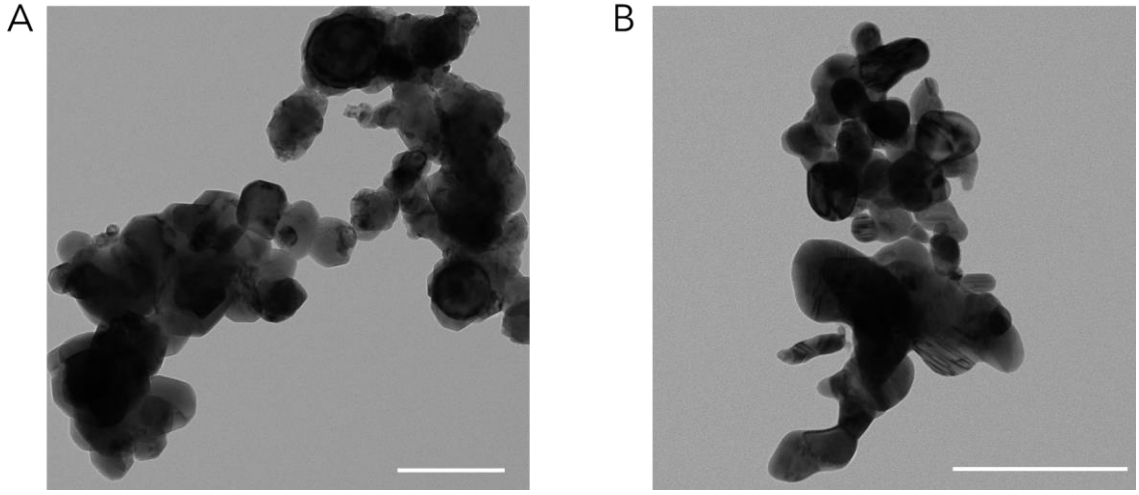

Figure S2. **Additional morphology characterization of commercial Cu and Ag powders.** (a) TEM image of commercial Cu (b) TEM image of commercial Ag. Scale bar: 200 nm.

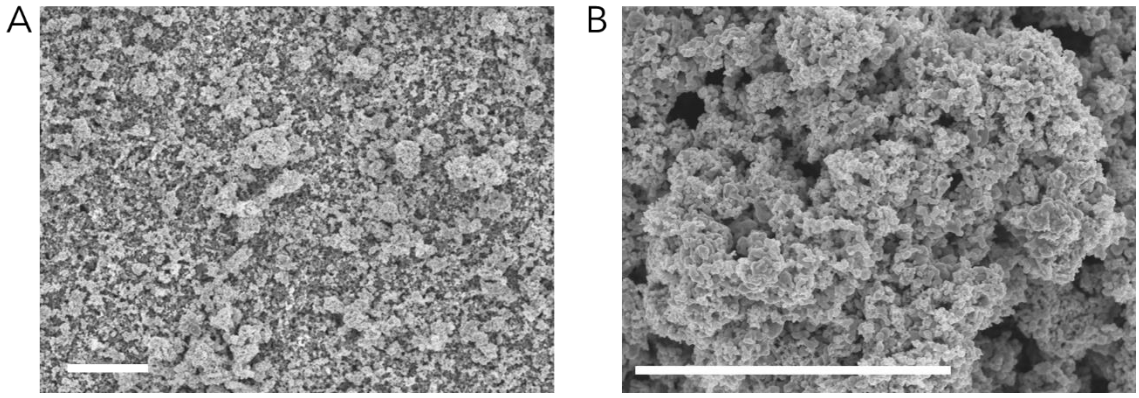

Figure S3. **SEM image of tandem $Cu_{500}Ag_{1000}$/carbon paper after electrolysis.** (a) low magnification and (b) high magnification SEM image of tandem $Cu_{500}Ag_{1000}$ catalyst after CO_2 electrolysis (30 min, 200 mA/cm^2, 1M KOH electrolyte). Scale bar: 2 μm.

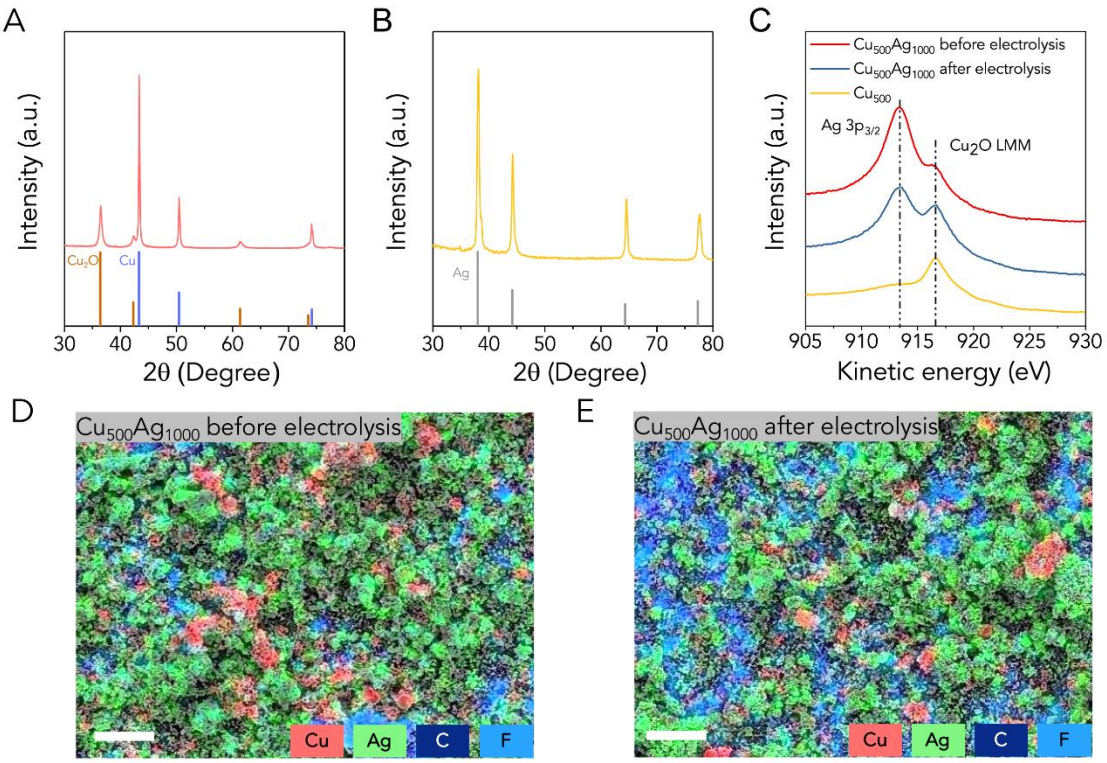

Figure S4. **Supplementary elemental characterization data.** (a) commercial Cu and (b) commercial Ag. Standard PDF index of Cu (ICDD PDF# 99-0034), Cu_2O (ICDD PDF# 99-0041), Ag (ICDD PDF# 99-0094) were also plotted for comparison. (c) LMM auger spectrum of tandem catalyst before and after electrolysis. Pure Cu catalyst was also characterized for reference. The auger peak of Cu_2O is partially overlapped with Ag $3p_{3/2}$. Both XRD and XPS data confirm the existence of Cu_2O at particle surface, likely due to surface oxidation. Elemental mapping of tandem $Cu_{500}Ag_{1000}$ catalyst (c) before and (d) after CO_2 electrolysis. Scale bar: 5 μm. Based on EDS elemental mapping, Cu and Ag powder were mixed at micron level, which is consistent with the TEM image in Fig S2. For $Cu_{500}Ag_{1000}$ catalyst, it can be observed that Cu and Ag are segregated both before and after CO_2 electrolysis. This offers additional supporting evidence for confirming the lack of bulky alloy formation.

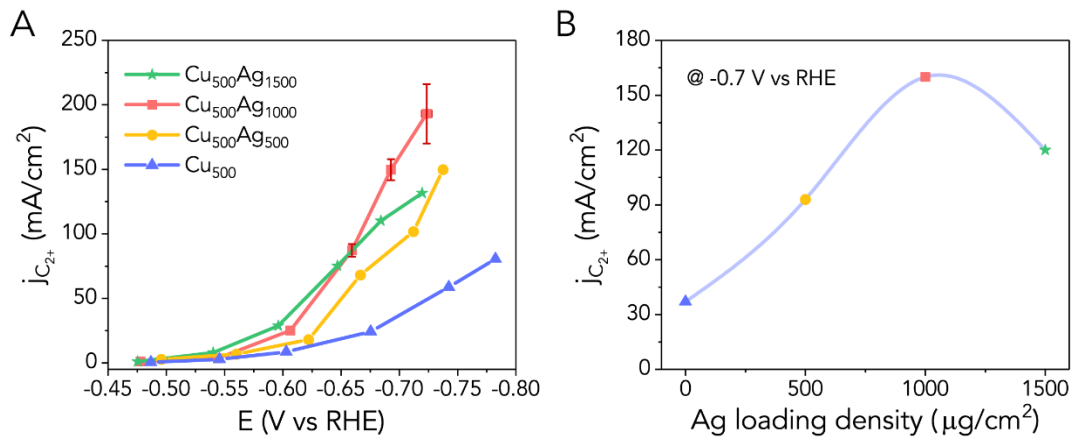

Figure S5. **Ag-loading dependent catalytic performance towards multicarbons over tandem catalysts.** (a) Partial current density towards C_{2+} products over tandem $Cu_{500}Ag_{1500}$, $Cu_{500}Ag_{1000}$, $Cu_{500}Ag_{500}$ and Cu_{500} catalysts in CO_2RR. (b) The relationship between Ag loading density in tandem catalyst and partial current density towards C_{2+} products at -0.70 V vs RHE. Partial current density values at -0.70 V vs RHE were obtained by linear interpolation. While Ag loading density below 1000 μg/cm^2, higher loading will result in larger C_{2+} partial current. But when Ag loading density exceed 1000 μg/cm^2, no further promotion could be observed, which may due to blockage of available Cu sites due to overcrowding of Ag.

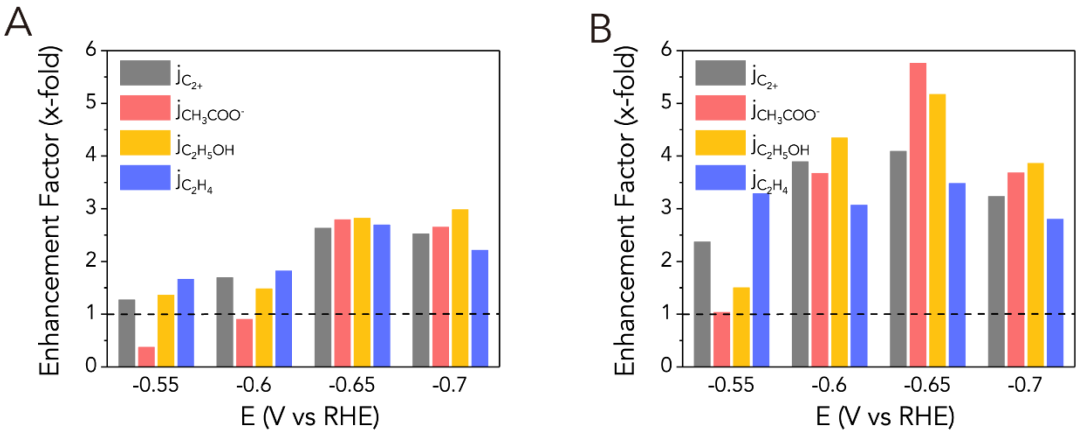

Figure S6. **Enhancement factors (EF) between (a) $Cu_{500}Ag_{500}$ and Cu_{500} (b) $Cu_{500}Ag_{1500}$ and Cu_{500} during CO_2RR, which is defined as the quotient of the partial currents between two catalysts.** Both total and specific C_{2+} products (C_2H_4, C_2H_5OH, $CH3COO^-$) EFs were calculated over four different potentials (-0.55V, -0.60V, -0.65V and -0.70V vs RHE). Linear interpolation was used to obtain the estimated current values at these potentials.

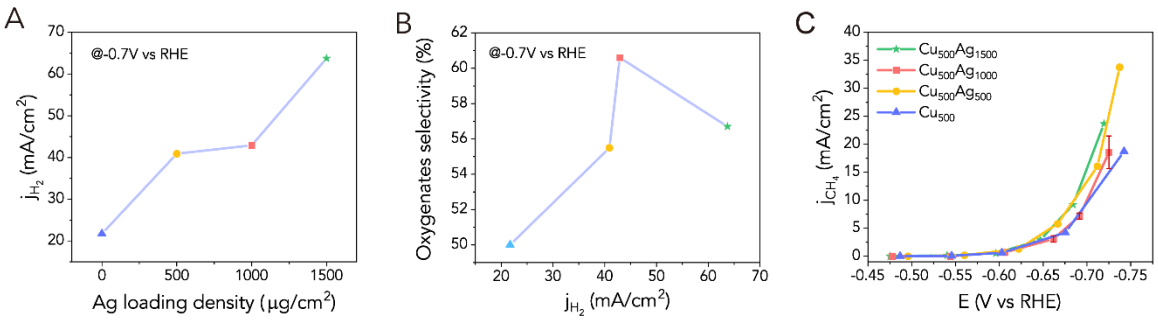

Figure S7. **Ag-loading dependent catalytic performance towards minor products over tandem catalysts.** (a) Partial current density towards H_2 over tandem $Cu_{500}Ag_{1500}$, $Cu_{500}Ag_{1000}$, $Cu_{500}Ag_{500}$ and Cu_{500} catalysts at -0.70 V vs RHE in CO_2RR. (b) The relationship between HER partial current density in tandem catalyst and oxygenates selectivity in multicarbon products at -0.70 V vs RHE. Partial current density values at -0.70 V vs RHE were obtained by linear interpolation. Generally, these results do not support a negative correlation between oxygenates selectivity and HER partial current density, which has been previously observed in Ag doped Cu catalyst[1]. Instead, a positive correlation can be found between Ag loading density and HER partial current density, suggesting a different mechanism for C_{2+} enhancement in this work relative to Ag-doped Cu works. (c) Partial current density towards CH_4 over tandem $Cu_{500}Ag_{1500}$, $Cu_{500}Ag_{1000}$, $Cu_{500}Ag_{500}$ and Cu_{500} catalysts in CO_2RR. The methane production rate seems to be independent with Ag loading density, which may suggest that methane production is not CO-limited.

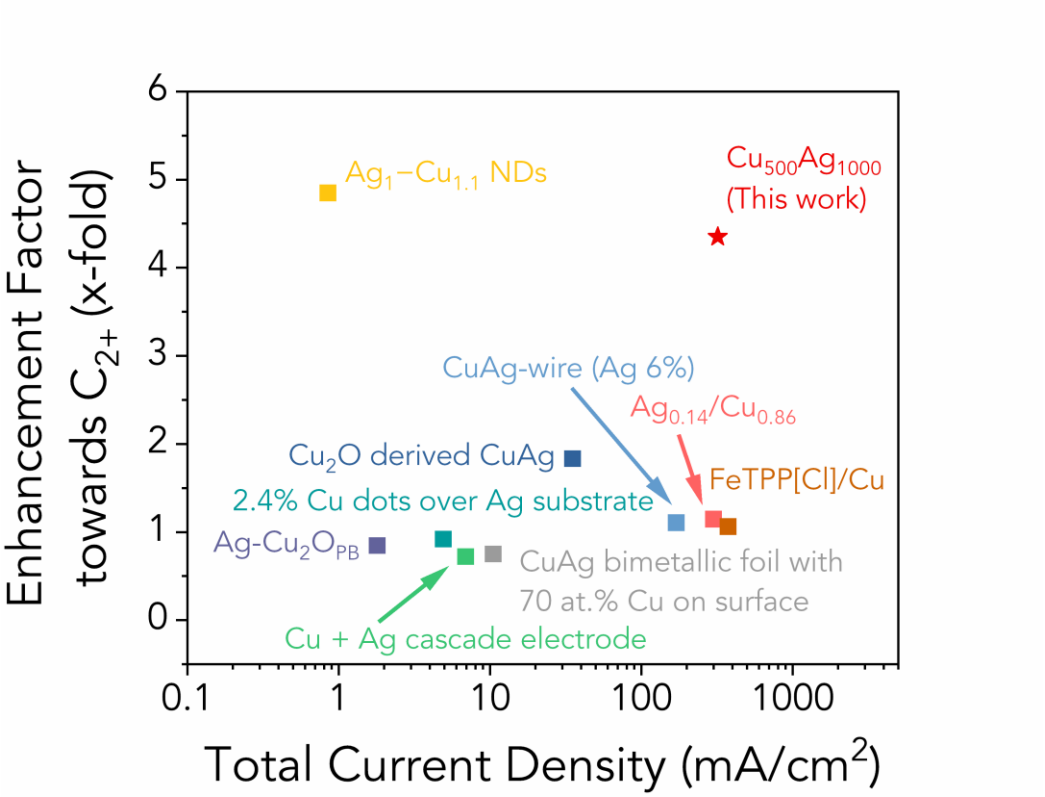

Figure S8. **Contextualization and comparison with relevant literature**. Total current density under most representative potential and the enhancement factors towards multicarbons are used as two indicators for comparison. More detailed information, including electrolyte, potential, total current density value and enhancement factors towards specific multicarbon products, can be found in table S1.

Although the alloying strategy (CuAg bimetallic foil; Ag0.14/Cu0.86; Ag-Cu2OPB) is a promising technique for tuning the selectivity of multicarbons, due to blockage of the surface, the value of EF towards total multicarbons are all around 1. Instead, tandem catalysts have a better potential to further improve EF (e.g. Cu2O derived CuAg). We attribute a higher EF in our work to the efficient CO-generating component in the catalyst (as compared with FeTPP[Cl] as an example) and high surface pH derived from electrolyte species and high electrolysis rate.

Note: (1) Enhancement factor (EF) here is defined as the quotient of partial current density between composed catalyst with reference pure Cu catalyst in literatures. Due to the varied morphology, ECSA and loading density of reference catalyst comparing with composed catalyst in some literatures, we remind readers of the potential imprecision contained in the calculated EF. (2) For the catalyst of $Ag_{0.14}/Cu_{0.86}$, offered comparison data are based on the same current density instead of same potential. (3) Due to the lack of same potential data, the product distribution under -0.84 V instead of -0.82 V vs RHE is used for the reference catalyst of FeTPP[Cl]/Cu.

Table S1. **Catalytic performance and enhancement factor comparison of relevant literatures**. The values of current densities were either offered in literature or extracted from the corresponding figures. Bottom half of table represents GDE works whereas top half represents H-cell.

Catalyst	Electrolyte	Potential (V vs RHE)	Total current density (mA/cm^2)	Enhancement factor			
				C_2H_4	C_2H_5OH	CH_3COOH & CH_3CHO	Total C_{2+}
CuAg bimetallic foil with 70 at.% Cu on surface[1]	0.1 M $CsHCO_3$	-1.05	10.1	0.6	1.2	4.5	0.8
Cu + Ag cascade electrode[2]	0.1 M $CsHCO_3$	-1.0	6.9	0.4	1.4	1.2	0.7
Ag-Cu_2O_{PB}[3]	0.2 M KCl	-1.2	1.8	0.3	1.9	0.9	0.9
2.4% Cu dots on Ag substrate[4]	0.1 M $KHCO_3$	-1.0	4.9	0.4	0.9	11.5	0.9
Cu_2O derived CuAg[5]	0.1 M $KHCO_3$	-1.05	35.1	2.1	1.3	1.5	1.8
Ag_1–$Cu_{1.1}$ NDs[6]	0.1 M $KHCO_3$	-1.1	0.85	4.9	N.A.	N.A.	4.9
$Ag_{0.14}/Cu_{0.86}$[7]	1 M KOH	N.A.	300	0.7	1.4	3.7	1.2
CuAg-wire (Ag 6%)[8]	1 M KOH	-0.6	170	1.3	0.9	0.8	1.1
FeTPP[Cl]/Cu[9]	1 M $KHCO_3$	-0.82	375	0.8	1.4	1.0	1.1
$Cu_{500}Ag_{1000}$ (This work)	1 M KOH	-0.7	320	3.4	5.5	5.3	4.4

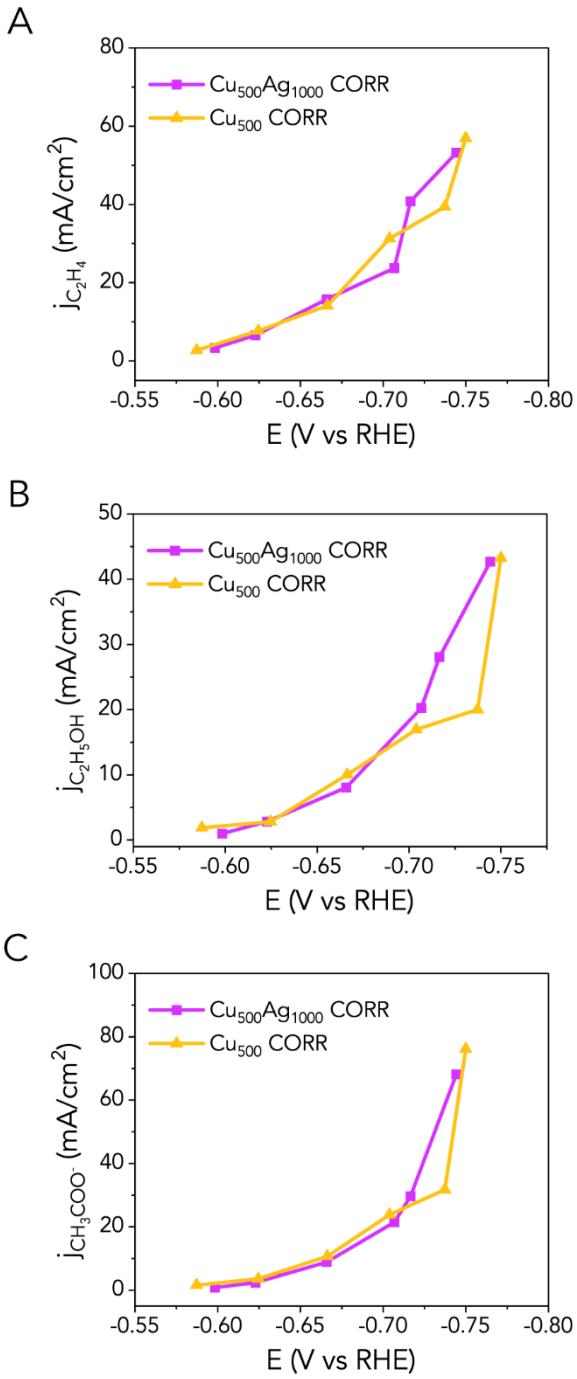

Figure S9. **Partial current density of (a) C_2H_4, (b) C_2H_5OH and (c) CH_3COO^- over both tandem $Cu_{500}Ag_{1000}$ and Cu_{500} catalyst in CORR.** No significant difference is observed.

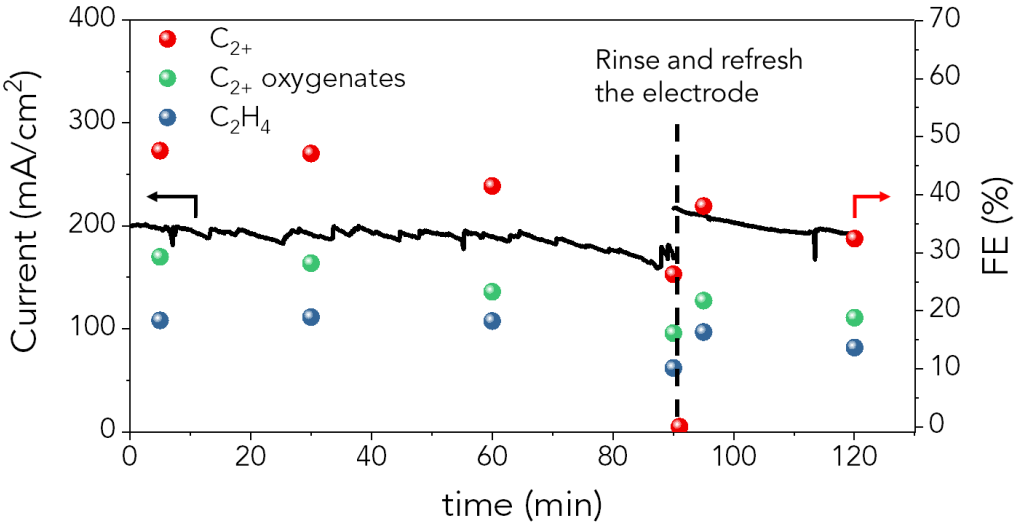

Figure S10. **Stability test under constant applied potential with 200 mA/cm^2 as starting current density.** The rapid catalytic deactivation happened after 1h electrolysis, which mainly due to the severe flood in gas diffusion layer. After the electrode fully deactivated, it was rinsed with DI water to remove electrolyte and precipitated out salts (*e.g.* K_2CO_3) thoroughly and then dried in vacuum chamber. The recovered catalytic activity during resumed CO_2 electrolysis indicates the deactivation mostly due to the instability of the carbon paper and the accumulation of carbonate salts from KOH-CO_2 reactivity.

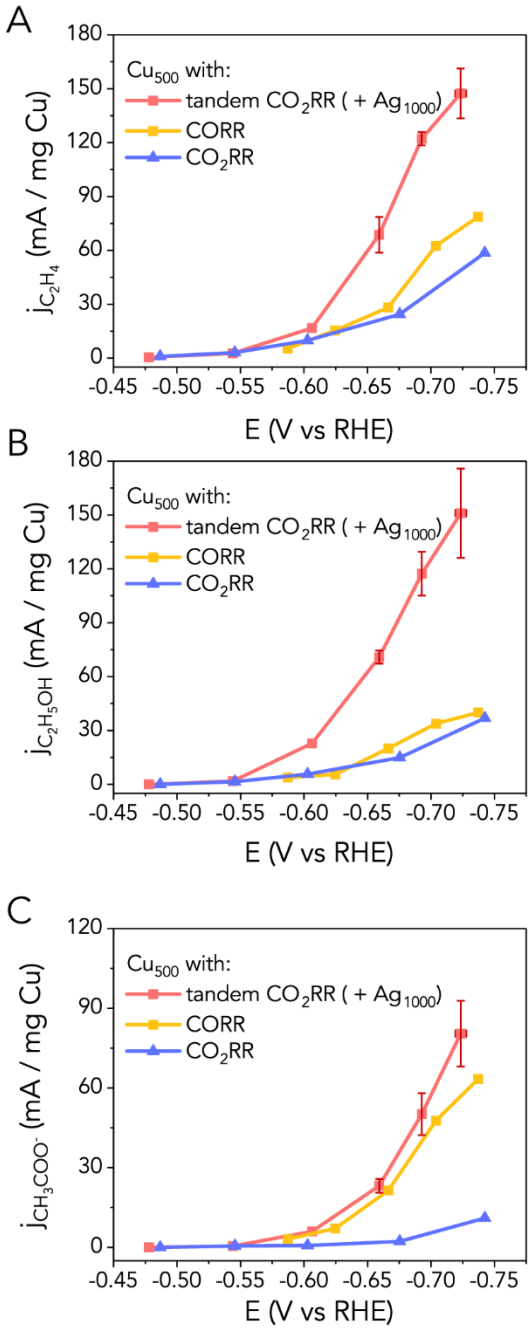

Figure S11. **Normalized partial currents towards (a) C_2H_4 (b) C_2H_5OH (c) CH_3COO^- over Cu_{500} surface with different local environments.**

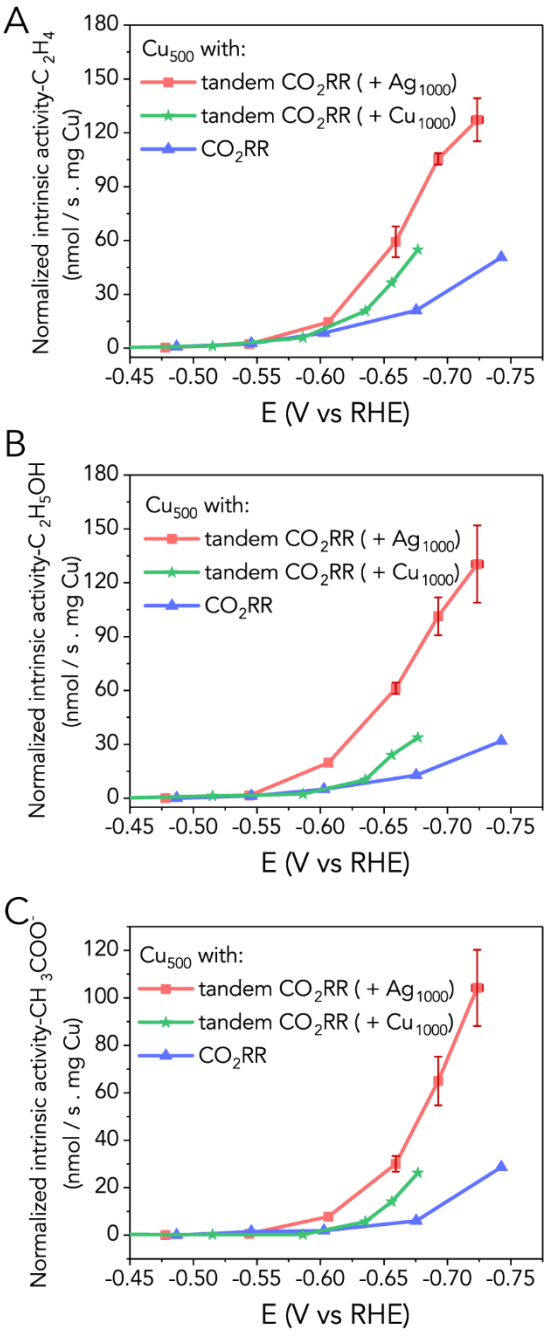

Figure S12. **Normalized intrinsic activity towards (a) C_2H_4 (b) C_2H_5OH (c) CH_3COO^- over $Cu_{500}Cu_{1000}$ in CO_2RR.** Cu_{500} and $Cu_{500}Ag_{1000}$ were also included for comparison.

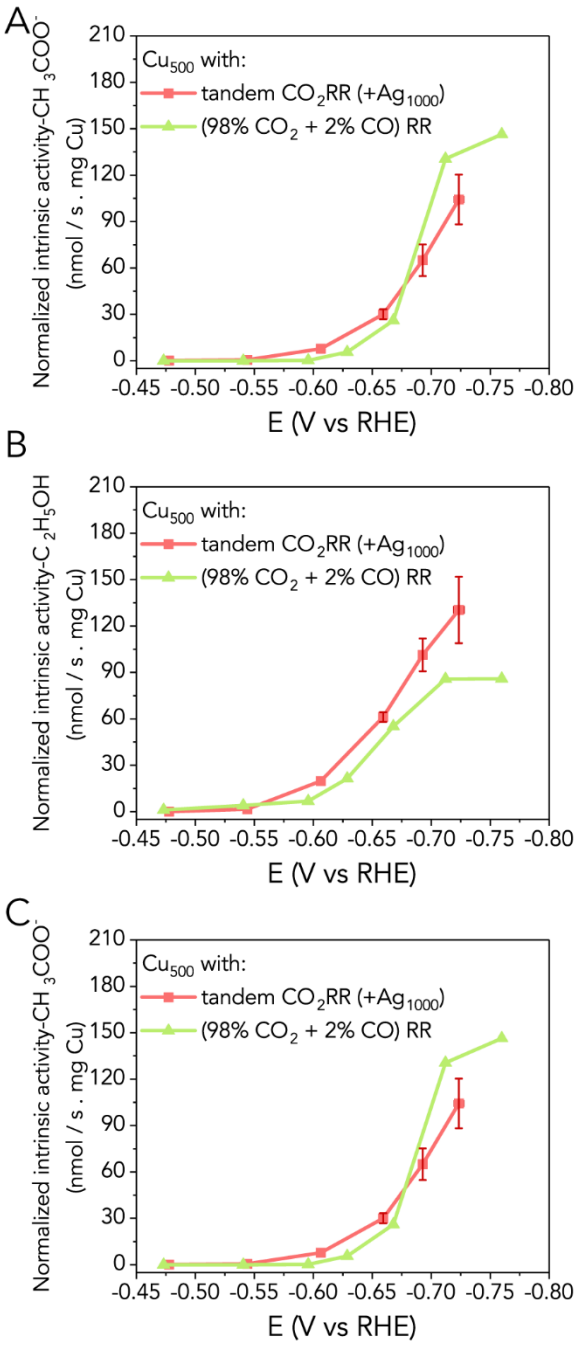

Figure S13. **Imitating tandem catalytic performance with a mixed gas of 2% CO and 98% CO_2.** Normalized intrinsic activity towards (a) C_2H_4 (b) C_2H_5OH (c) CH_3COO^- over Cu_{500} in a mixed gas atmosphere with 98% CO_2 and 2% CO. $Cu_{500}Ag_{1000}$ CO_2RR data were also included for comparison. Under comparable CO partial pressure, a similar intrinsic activity enhancement could also be observed on Cu_{500}, indicating the correlation between increased performance and the co-existence of CO and CO_2.

References:

(1) Clark, E. L.; Hahn, C.; Jaramillo, T. F. and Bell, A. T., (2017). Electrochemical CO2 Reduction over

Compressively Strained CuAg Surface Alloys with Enhanced Multi-Carbon Oxygenate Selectivity. J. Am. Chem. Soc. *139*, 15848-15857.

(2) Gurudayal, G.; Perone, D.; Malani, S.; Lum, Y.; Haussener, S. and Ager, J. W., (2019). Sequential Cascade Electrocatalytic Conversion of Carbon Dioxide to CC Coupled Products. ACS Appl. Energy Mater. *2*, 4551-4559.

(3) Lee, S.; Park, G. and Lee, J., (2017). Importance of Ag–Cu biphasic boundaries for selective electrochemical reduction of CO2 to ethanol. ACS catal. *7*, 8594-8604.

(4) Lum, Y. and Ager, J. W., (2018). Sequential catalysis controls selectivity in electrochemical CO2 reduction on Cu. Energy Environ. Sci. *11*, 2935-2944.

(5) Gao, J.; Zhang, H.; Guo, X.; Luo, J.; Zakeeruddin, S. M.; Ren, D. and Grätzel, M., (2019). Selective C–C Coupling in Carbon Dioxide Electroreduction via Efficient Spillover of Intermediates As Supported by Operando Raman Spectroscopy. J. Am. Chem. Soc. *141*, 18704-18714.

(6) Huang, J.; Mensi, M.; Oveisi, E.; Mantella, V. and Buonsanti, R., (2019). Structural Sensitivities in Bimetallic Catalysts for Electrochemical CO2 Reduction Revealed by Ag-Cu Nanodimers. J. Am. Chem. Soc. *141*, 2490-2499.

(7) Li, Y. C.; Wang, Z.; Yuan, T.; Nam, D. H.; Luo, M.; Wicks, J.; Chen, B.; Li, J.; Li, F.; de Arquer, F. P. G.; Wang, Y.; Dinh, C. T.; Voznyy, O.; Sinton, D. and Sargent, E. H., (2019). Binding Site Diversity Promotes CO2 Electroreduction to Ethanol. J. Am. Chem. Soc. *141*, 8584-8591.

(8) Hoang, T. T. H.; Verma, S.; Ma, S.; Fister, T. T.; Timoshenko, J.; Frenkel, A. I.; Kenis, P. J. A. and Gewirth, A. A., (2018). Nanoporous Copper-Silver Alloys by Additive-Controlled Electrodeposition for the Selective Electroreduction of CO2 to Ethylene and Ethanol. J. Am. Chem. Soc. *140*, 5791-5797.

(9) Li, F.; Li, Y. C.; Wang, Z.; Li, J.; Nam, D.-H.; Lum, Y.; Luo, M.; Wang, X.; Ozden, A.; Hung, S.-F.; Chen, B.; Wang, Y.; Wicks, J.; Xu, Y.; Li, Y.; Gabardo, C. M.; Dinh, C.-T.; Wang, Y.; Zhuang, T.-T.; Sinton, D. and Sargent, E. H., (2019). Cooperative CO2-to-ethanol conversion via enriched intermediates at molecule–metal catalyst interfaces. Nat. Catal. *3*, 75-82.